High Mobility, Hole Transport Materials for Highly Efficient PEDOT:PSS Replacement in Inverted Perovskite Solar Cells

Marios Neophytou[†], Jack Griffiths[†Δ], James Fraser[†Δ], Mindaugas Kirkus[†], Hu Chen[†], Christian B. Nielsen[§] and Iain McCulloch[†‡]

[†] King Abdullah University of Science and Technology, KAUST Solar Centre, Physical Science and Engineering Department, Thuwal 23955-6900, Saudi Arabia

[Δ] WestCHEM, School of Chemistry, University of Glasgow, Joseph Black Building, University Avenue, Glasgow G128QQ, United Kingdom

[‡]Department of Chemistry and Centre for Plastic Electronics, Imperial College London, South Kensington Campus, SW7 2AZ, United Kingdom

[§] Materials Research Institute and School of Biological and Chemical Sciences, Queen Mary University of London, Mile End Road, London E1 4NS, United Kingdom

Perovskite solar cells (PSCs) have gained recognition as one of the most promising photovoltaic technologies due to their remarkable increase in power conversion efficiency (PCE) from 3.8% to 21.1% in a short period of time [1, 2]. The main component of the majority of perovskite solar cells up till now have been organic amine lead halide derivatives with ABX_3 perovskite structure (A: $(CH_3NH_3)^+$, B: Pb_2^+, X: Cl^-, Br^- or I^-). More recently, the methyl ammonium ion is being replaced with more stable counterions such as caesium cation due to increased thermal and structural stability [3, 4]. Perovskites have several advantageous properties, which contribute to their impressive performance, including: high light absorption [5, 6], good charge mobility [7, 8] and small exciton binding energy [9]. The inverted device structure usually comprises of two organic charge transport layers, [6,6]-phenyl-C_{61}-butyric acid methyl ester (PCBM) as the electron transporting material and poly(3,4-ethylenedioxythiophene) polystyrene sulfonate(PEDOT:PSS) as the hole transporting layer. Inverted architecture devices can be processed at relatively low temperatures (~120 °C) [10] compatible with flexible substrates. Therefore PSCs show potential to be manufactured at a low cost [11, 12] and at an industrial scale. The main drawback to this type of device architecture is the inclusion of PEDOT:PSS as the HTL, which is not

optimal due to its inefficient electron-blocking properties and limited chemical stability arising from its acidity and highly hygroscopic nature [13-15]. Replacing PEDOT:PSS with a more stable HTL is therefore a viable option to improve inverted perovskite devices. New hole transporting materials must be easily synthetically scalable, soluble in a variety of process compatible solvents and have excellent electron blocking and hole transporting properties, exhibiting at the same time high charge carrier mobilities.

In this case we report the application of two solution processed triarylamine based small molecule semiconductors easily synthesised from common starting materials. Triarylamines have been utilised extensively in organic light emitting diodes (OLEDs)[16, 17] organic field-effect transistors (OFETs) [18] and photovoltaics [19] due to their excellent transport properties, thermal and chemical stability but also their suitable highest occupied molecular orbital (HOMO) in relation to methylammonium lead iodide perovskite semiconductor valence band. Usually these triarylamines are used to flank a central core, with little through conjugation, which allows for tuning of the optoelectronic properties of the molecule by changing the substituents upon the arylamine. In this case we chose biphenyl and naphthalene as the central cores flanked by two N,N-bis(4-methoxyphenyl)aniline groups as shown in figure 1a, along with calculated density functional theory (DFT) measurements. Complete structural and thermal characterisation were performed using standard techniques including ^{1}H NMR, ^{13}C NMR and thermal gravimetric analysis and differential scanning calorimetry (TGA/DSC). Detailed synthetic methods and characterisation are included in the supporting information section.
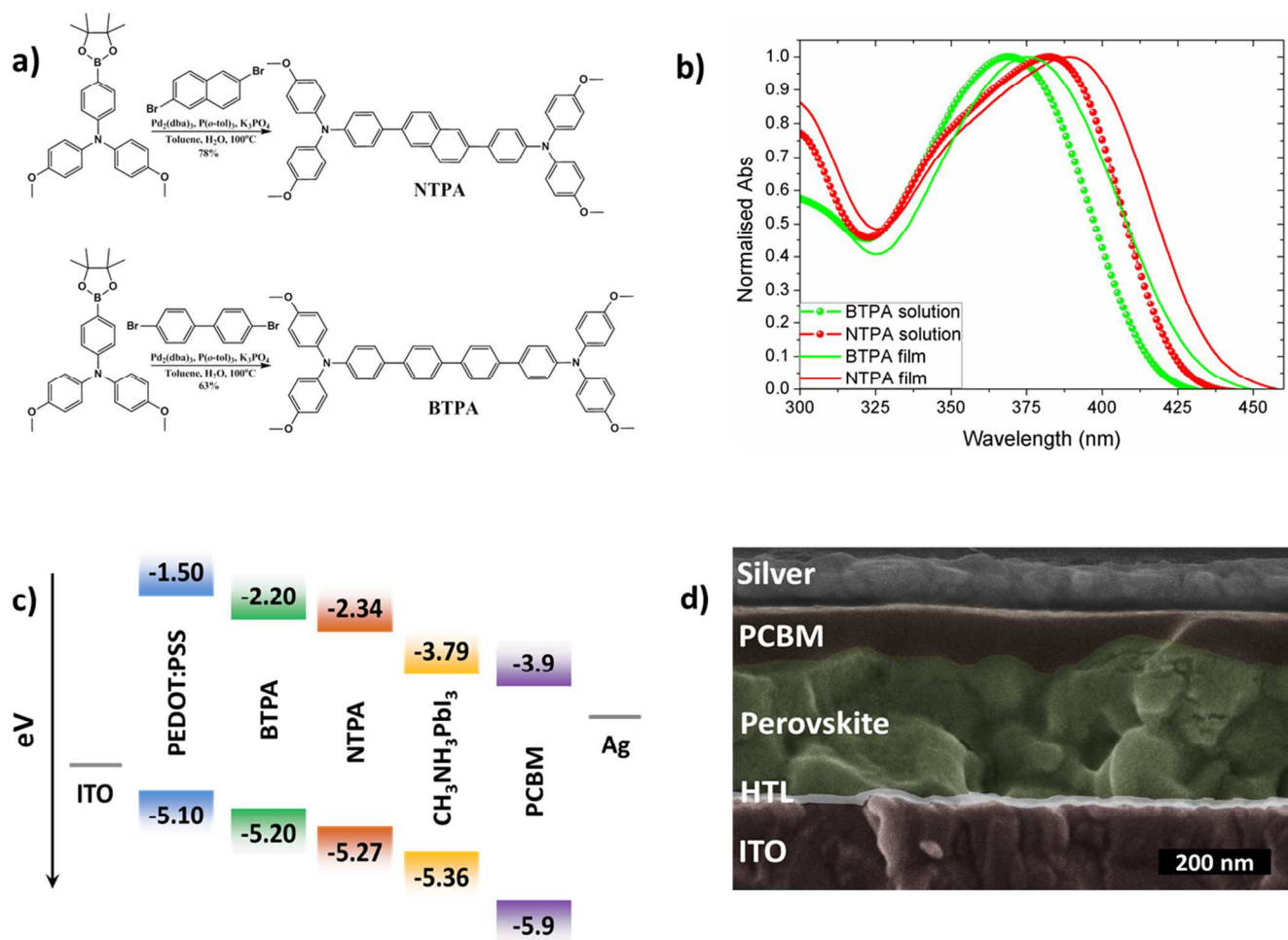
Figure 1: Chemical structures (a) and UV-Vis absorption spectra of the two novel HTMs (b), energy level diagram of the compounds (c), cross-sectional SEM image of the device stack (d)

Table 1: Opto-electronic data of NTPA and BTPA

HTM	λ_{abs} film/nm	λ_{abs} solution/nm	$E_{opt.gap}$[a] (E_g)	Ionization Potential (IP) (eV)[b]	Electron Affinity (eV)[c]
NTPA	391	386	2.93	5.27	2.34
BTPA	375	369	3.00	5.20	2.20

[a]obtained from the onset value of absorption.

[b]measured by Photo-Electron Spectroscopy in Air (PESA) system.

[c]calculated from E_g and IP.

UV-Vis absorption data of both thin-film and solution for NTPA and BTPA were obtained, and shown in Figure 1b. A red shift between solution and film is observed, which is indicative of increased aggregation in thin film layers with stronger $\pi \rightarrow \pi^*$ transitions, hence decreasing the optical band gap (E_g). Ionization potential values for PEDOT:PSS, NTPA and BTPA were obtained with Photo-Electron Spectroscopy in Air (PSEA). When the optical band gap (E_g) is subtracted from those values electron affinities can be estimated. The experimental data is summarised in Table 1. The IP of NTPA and BTPA are -5.27 eV and -5.20 eV respectively, and as both lie between the IP of the perovskite (-5.36 eV) and the work function of ITO (-4.76 eV), both molecules can provide sufficient hole extraction capabilities within the PSC. The electron affinities give an indication of the LUMO, lying at -2.34 eV and -2.20 eV for NTPA and BTPA respectively. Both are sufficiently high enough to provide an electron blocking function between the perovskite photoactive layer and ITO within the PSC. It should be noted that that stated electron affinity of PEDOT:PSS is based upon optical data obtained, however PEDOT:PSS contains intraband states due to the PSS dopant and polymer organisation in the solid state exhibiting a semi-metallic state [20, 21]. This allows electron transfer between the perovskite semiconductor absorbing

layer and the ITO electrode, where charge recombination can occur; inhibiting device performance. The respective energy levels are schematically depicted in figure 1c. A cross-sectional scanning electron microscopy (SEM) image shows the fully optimized champion device employing NTPA as the hole transporting layer (HTL) in figure 1d. The p-type NTPA or BTPA and n-type PCBM transporting layers sandwich the $CH_3NH_3PbI_3$ perovskite absorbing layer. As shown in the SEM image, the HTL is of very low thickness, on the order of tens of nanometres, which was determined by scanning profilometry; the layers in the cross-section have been post-imaging coloured to add increased layer contrast.

In order to determine charge carrier mobility for the NTPA and BTPA, hole-only devices were fabricated with structure ITO/HTL/MoOx/Ag, where the devices were tested under similar conditions to that of the optimised photovoltaic devices.

Hole mobilities were extracted using the modified Mott-Gurney equation below:

$$J_{SCLC} = \frac{9}{8}\varepsilon_0\varepsilon_r\mu\frac{V_{in}^2}{L^3}e^{\left(\frac{0.89\beta}{\sqrt{L}}\sqrt{V_{in}}\right)}$$

where J_{SCLC} is the measured current density, ε_0 and ε_r are defined as the vacuum permittivity and material dielectric constant respectively, L is the film thickness, μ the hole mobility, and β is the field activation parameter. A significant change in mobility was observed between as deposited and annealed HTLs, 8.8 x 10^{-5} $cm^2 V^{-1} s^{-1}$ and 1.1x 10^{-3} $cm^2 V^{-1} s^{-1}$ respectively for NTPA and 8.1 x 10^{-5} $cm^2 V^{-1} s^{-1}$ and 4.7 x 10^{-4} $cm^2 V^{-1} s^{-1}$ respectively for BTPA; shown in figure S5. These values are higher than mobilities of un-doped Spiro-oMeTAD, PTAA (polytriarylamine) compounds and other HTMs reported in the literature [22-24].
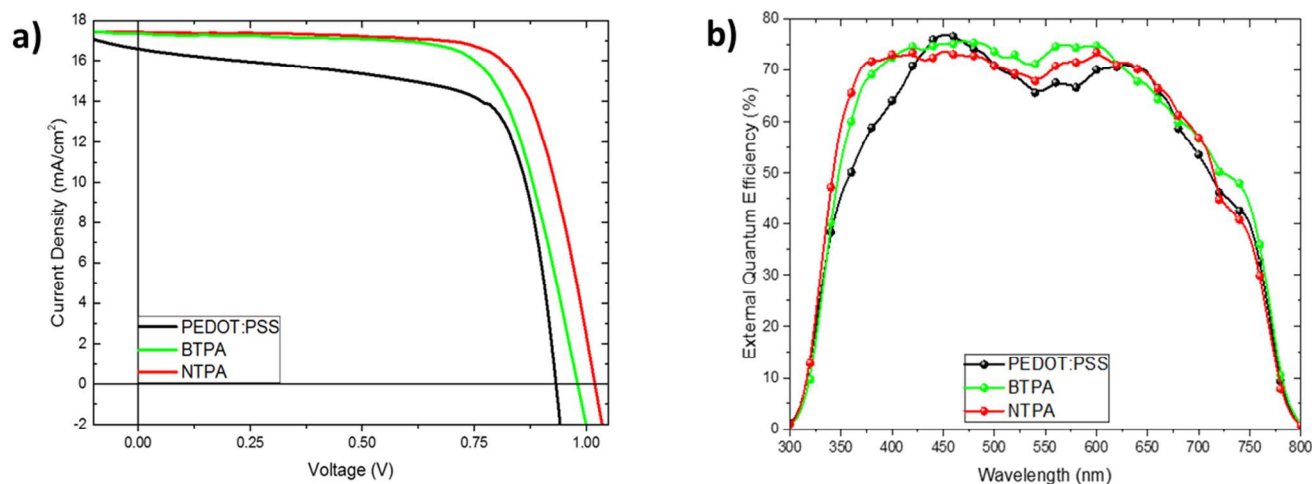
Figure 2: J-V characteristics (a) and respective EQE spectra (b) of perovskite devices utilizing novel HTMs and PEDOT:PSS as reference.

The incorporation of high mobility cores, as previously mentioned, which can assemble in close packed arrangements, allows for a high degree of intermolecular charge transfer and hence a higher charge carrier mobility [25]. The preferential molecular tuning of small molecules over polymer units allowed for the addition of finely tuned triarylamines; providing the optimized energy levels for hole transfer and extraction. Comparing the AFM images between the NTPA and BTPA molecules (Figure S6), the former shows an increase in surface roughness. This may be indicative of larger crystalline domains post annealing; accounting for the higher mobility observed in NTPA films. Additionally, it has been previously demonstrated by Bi et. al. that growth of perovskite grains with high aspect ratio on non-wetting HTLs can be achieved by solution based methods; allowing for thin film solar cells demonstrating reduced charge recombination at grain boundaries [26]. Contact angle measurements (Figure S10) demonstrated that both NTPA and BTPA are hydrophobic, which assisted the development of perovskite crystal films with larger aspect ratios than with PEDOT:PSS, as shown by top view SEM

images (Figures 3a-c), with perovskite crystal domains increase in size moving from PEDOT:PSS<BTPA<NTPA.

In order to further analyze the crystal size, X-ray diffraction measurements were performed on perovskite films coated on top of HTLs. Peaks at 14.27° and 28.58° 2θ-angles are associated with (110) and (220) crystal planes of perovskite, as indicated on figure 3d. Both NTPA and BTPA based perovskite layers exhibit higher peak intensities in comparison to patterns obtained with PEDOT:PSS as the hole transporting material, suggesting the presence of larger crystalline domains (Figure 3d inset), which facilitates the ability for higher charge carrier density (J_{SC}) and fill factor (FF), a statement also supported by top view SEM and J/V characteristics.
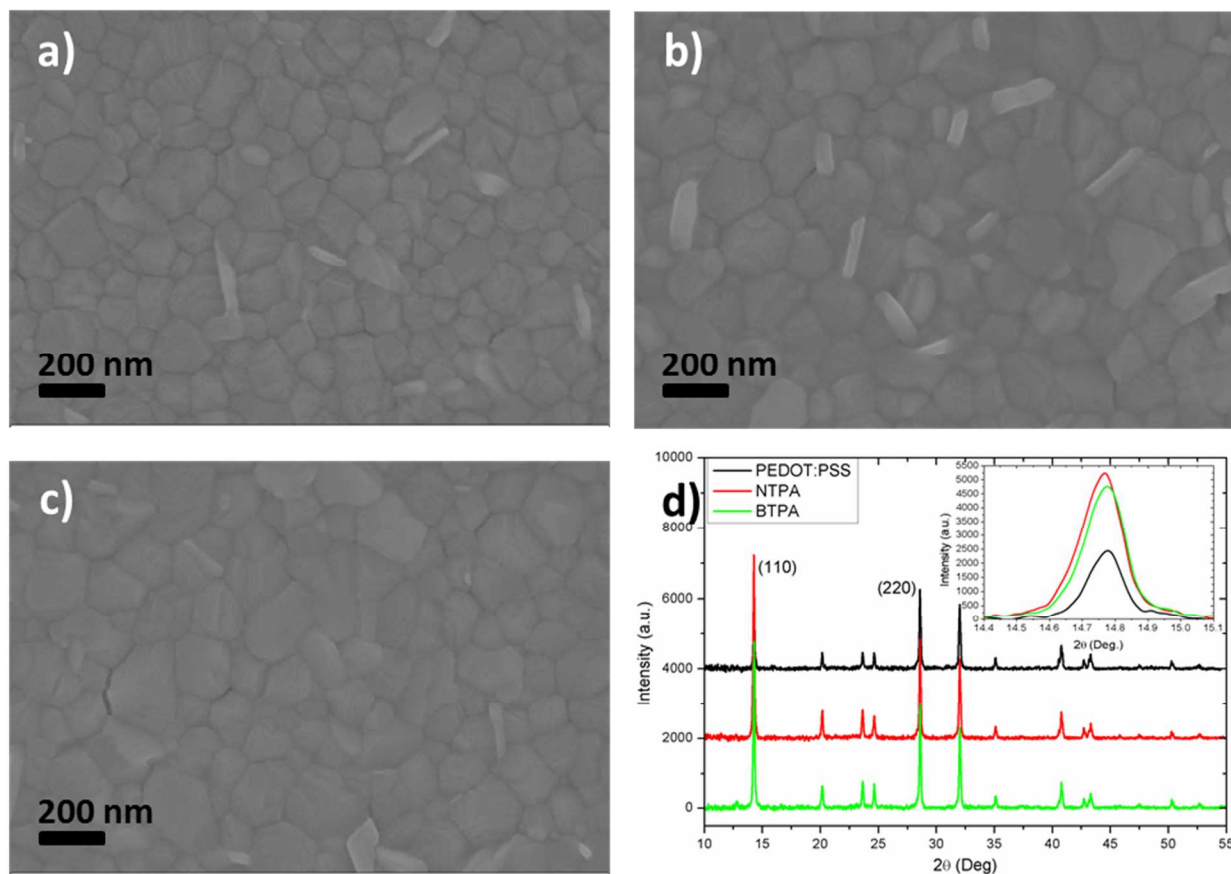
Figure 3: Top view SEM images of perovskite layers coated on top of a) PEDOT:PSS, b) BTPA and c) NTPA. D) X-ray diffraction pattern of perovskite deposited different HTMs.

Density Functional Theory (DFT) calculations using the B3LYP/6–31g* basis set (Figure S11) are in excellent agreement with experimental data concerning high lying LUMOs for NTPA and BTPA molecules explaining favourable electron blocking properties. The latter, in combination with high hole mobility values, creates the potential for these HTMs to exhibit high device performance, when replacing PEDOT:PSS in a PSC. Devices were fabricated with a typical inverted structure, with the device architecture depicted in Figure 1d. The HTL was spin coated from a chlorobenzene solution onto an ITO-coated substrate, PEDOT:PSS was used as purchased in aqueous solution. The optimization process of the HTL involved both thickness variation and thermal annealing effects. The perovskite

layer was deposited using a one-step, fast crystallization method. Subsequently, PCBM was deposited via spin coating from chlorobenzene with a final 100 nm of silver deposited on top of the device structure via thermal evaporation. Optimal layer thicknesses were determined to be ~30 nm of the HTL, 70 nm for the PCBM and 200 nm for the $CH_3NH_3PbI_3$, which is in accordance with literature [27, 28]. The devices were tested under calibrated AM1.5G solar illumination, where device performance of the new HTL materials was shown to outperform that of PEDOT:PSS reference device. The processing steps for full device fabrication is available in the supporting material.

Figure 2a shows current density vs voltage (J-V) characteristics of the photovoltaic devices employing NTPA, BTPA and PEDOT:PSS as HTLs. Device performance showed little variation when statistically analysed (Figure S3a,b), indicating good reproducibility with maximum obtained power conversion efficiency of 13.0% and 12.1% for NTPA and BTPA devices respectively. Table 2 summarizes the champion device performance of each HTL. Obtained J_{sc} values for both NTPA and BTPA significantly exceed that of PEDOT:PSS. This is likely due to the enhanced electron blocking properties and the high charge carrier mobilities along with reduction in charge recombination due to larger average perovskite grain size for the novel HTM based devices over PEDOT:PSS devices. The new HTMs allow for a greater degree of charge extraction and hence improved J_{SC}. This is also evident in the EQE data (figure 2b). EQE curves of the newly synthesized HTM based devices, when compared to those with PEDOT:PSS exhibit higher current generation in the UV region. Devices made with NTPA and BTPA exhibit no pronounced differences, with quantum efficiency reaching values in the region of 75%. In line with this increased J_{sc} when average device statistics were analysed an increased fill factor was observed due to high charge carrier mobilities and electron blocking ability of the two novel

synthesised HTMs. The V_{oc} values are concordant with the determined IPs with NTPA providing the greatest V_{oc} and lowest IP, followed by BTPA and PEDOT:PSS respectively. As shown in S.I. the devices shows some hysteresis (Figure S1), with power conversion efficiency (PCE) values lacking in the reverse to forward bias (RB-FB) measurement when compared to that of the forward to reverse bias (FB-RB). This decrease is mainly attributed to fill factor reduction from 70.8% to 63.7% for NTPA and 73.3% to 66.5% for BTPA based perovskite devices. Hysteresis has been shown to be significantly influenced by time-dependant capacitive current [29]. Furthermore device stability was measured at maximum power point over 60 seconds (Figure S2) and showed no degradation; indicating a stable perovskite layer, with the ability for continual charge extraction. Over 50 devices were fabricated and were statistically consistent to the champion devices with minimal variation as shown in Figure S3.

Table 2: Champion photovoltaic device performance

Device	J_{sc} (mA/cm^2)	V_{oc} (V)	FF (%)	PCE (%)	R_{shunt} kΩ cm^2	R_{series} Ω cm^2
PEDOT:PSS	16.7 (16.1)[*]	0.93	70.0	10.9	9	1.9
BTPA FB-RB	17.4 (16.9)[*]	0.98	70.8	12.1	15	7.3
RB-FB	17.3	0.98	63.7	10.8		
NTPA FB-RB	17.4 (17.0)[*]	1.02	73.3	13.0	32	5.7
RB-FB	16.9	1.02	66.5	11.4		

[*] Jsc calculated from EQE

PEDOT:PSS based devices show a deficiency in shunt resistance (R_{shunt}) when compared to BTPA and NTPA, with calculated values around 9, 15 and 32 kΩ.cm^2 as shown in Table 2. Alternative current pathways are present in the device and bimolecular recombination of charge carriers may occur. As already discussed, PEDOT:PSS inability for efficient electron blocking, as well as pin-hole formation at

the ITO/PEDOT:PSS interface highlights the need for novel HTL materials. Relatively low series resistance (R_{series}), was observed for the new HTM based devices and mainly attributed to high hole mobility, due to favourable packing of the molecules. Lifetime evaluation of perovskite solar cell devices without any encapsulation employing NTPA and BTPA, was performed over a period of time (Figure S4). Devices were stored in a nitrogen glovebox and even after 30 days, device performance for both HTLs exhibited only a small reduction of less than 15%. This strongly suggests the suitability of these novel HTLs for more stable and long lasting perovskite devices.

In conclusion, high mobility HTM molecules, in the order of 10^{-3} V/cm.s and strong electron blocking properties in molecular design have been shown to improve device performance over PEDOT:PSS, in an inverted perovskite structure. Power conversion efficiencies of 13.0% and 12.1% were achieved for NTPA and BTPA respectively, which are easily solution processed at low temperatures with high stability, lifetime in excess of 500 hours and low material cost provide the potential for future scalable processes and application on the flexible substrates in large scale perovskite solar cells.

References

1.   Kojima, A.; Teshima, K.; Shirai, Y.; Miyasaka, T., Organometal Halide Perovskites as Visible-Light Sensitizers for Photovoltaic Cells. *Journal of the Americal Chemical Society* **2009,** *131* (17), 6050-6051.
2.   Saliba, M.; Matsui, T.; Seo, J.-Y.; Domanski, K.; Correa-Baena, J.-P.; Nazeeruddin, M. K.; Zakeeruddin, S. M.; Tress, W.; Abate, A.; Hagfeldt, A.; Grätzel, M., Cesium-containing triple cation perovskite solar cells: improved stability, reproducibility and high efficiency. *Energy & Environmental Science* **2016,** *9*, 1989-1997.
3.   Sutton, R. J.; Eperon, G. E.; Miranda, L.; Parrott, E. S.; Kamino, B. A.; Patel, J. B.; Hörantner, M. T.; Johnston, M. B.; Haghighirad, A. A.; Moore, D. T.; Snaith, H. J., Bandgap-Tunable Cesium Lead Halide Perovskites with High Thermal Stability for Efficient Solar Cells. *Advanced Energy Materials* **2016,** *6* (8), 1502458.
4.   McMeekin, D. P.; Sadoughi, G.; Rehman, W.; Eperon, G. E.; Saliba, M.; Hörantner, M. T.; Haghighirad, A.; Sakai, N.; Korte, L.; Rech, B.; Johnston, M. B.; Herz, L. M.; Snaith, H. J., A mixed-cation lead mixed-halide perovskite absorber for tandem solar cells. *Science* **2016,** *351* (6269), 151-155.
5.   Kim, H.-S.; Lee, C.-R.; Im, J.-H.; Lee, K.-B.; Moehl, T.; Marchioro, A.; Moon, S.-J.; Humphry-Baker, R.; Yum, J.-H.; Moser, J. E.; Grätzel, M.; Park, N.-G., Lead Iodide Perovskite Sensitized All-Solid-State Submicron Thin Film Mesoscopic Solar Cell with Efficiency Exceeding 9%. *Scientific Reports* **2012,** *2*, 591.
6.   Park, N.-G., Organometal Perovskite Light Absorbers Toward a 20% Efficiency Low-Cost Solid-State Mesoscopic Solar Cell. *Journal of Physical Chemistry Letters* **2013,** *4* (15), 2423-2429.
7.   Malinkiewicz, O.; Yella, A.; Lee, Y. H.; Espallargas, G. M.; Graetzel, M.; Nazeeruddin, M. K.; Bolink, H. J., Perovskite solar cells employing organic charge-transport layers. *Nature Photonics* **2013,** *8*, 128-132.
8.   Kazim, S.; Nazeeruddin, M. K.; Grätzel, M.; Ahmad, S., Perovskite as Light Harvester: A Game Changer in Photovoltaics. *Angewandte Chemie International Edition* **2014,** *53* (11), 2812-2824.
9.   Park, S.; Heo, J. H.; Cheon, C. H.; Kim, H.; Im, S. H.; Son, H. J., A [2,2]paracyclophane triarylamine-based hole-transporting material for high performance perovskite solar cells. *Journal of Materials Chemistry A* **2015,** *3*, 24215-24220.
10.   Xiao, Z.; Bi, C.; Shao, Y.; Dong, Q.; Wang, Q.; Yuan, Y.; Wang, C.; Gao, Y.; Huang, J., Efficient, high yield perovskite photovoltaic devices grown by interdiffusion of solution-processed precursor stacking layers. *Energy and Environmental Science* **2014,** *7*, 2619-2623.
11.   Li, H.; Fu, K.; Boix, P. P.; Wong, L. H.; Hagfeldt, A.; Grätzel, M.; Mhaisalkar, S. G.; Grimsdale, A. C., Hole-Transporting Small Molecules Based on Thiophene Cores for High Efficiency Perovskite Solar Cells. *ChemSusChem* **2014,** *7* (12), 3420-3425.
12.   Chen, H.; Bryant, D.; Troughton, J.; Kirkus, M.; Neophytou, M.; Miao, X.; Durrant, J. R.; McCulloch, I., One-Step Facile Synthesis of a Simple Hole Transport Material for Efficient Perovskite Solar Cells. *Chemistry of Materials* **2016,** *28* (8), 2515–2518.
13.   Ye, S.; Sun, W.; Li, Y.; Yan, W.; Peng, H.; Bian, Z.; Liu, Z.; Huang, C., CuSCN-Based Inverted Planar Perovskite Solar Cell with an Average PCE of 15.6%. *Nano Letters* **2015,** *15* (6), 3723-3728.
14.   Labban, A. E.; Chen, H.; Kirkus, M.; Barbe, J.; Del Gobbo, S.; Neophytou, M.; McCulloch, I., Improved Efficiency in Inverted Perovskite Solar Cells Employing a Novel Diarylamino-Substituted Molecule as PEDOT:PSS Replacement. *Advanced Energy Materials* **2016,** 1502101.
15.   Lee, W.; Song, M.; Park, S.; Nam, S.; Seo, J.; Kim, H.; Kim, Y., Acidity-Controlled Conducting Polymer Films for Organic Thermoelectric Devices with Horizontal and Vertical Architectures. *Scientific Reports* **2016,** *6*, 33795.
16.   Jiang, Z.; Ye, T.; Yang, C.; Yang, D.; Zhu, M.; Zhong, C.; Qin, J.; Ma, D., Star-Shaped Oligotriarylamines with Planarized Triphenylamine Core: Solution-Processable, High-Tg Hole-Injecting and Hole-Transporting Materials for Organic Light-Emitting Devices†. *Chemistry of Materials* **2011,** *23* (3), 771-777.
17.   Thelakkat, M., Star-Shaped, Dendrimeric and Polymeric Triarylamines as Photoconductors and Hole Transport Materials for Electro-Optical Applications. *Macromolecular Materials and Engineering* **2002,** *287* (7), 442-461.

18.   Schelter, J.; Mielke, G. F.; Köhnen, A.; Wies, J.; Köber, S.; Nuyken, O., Novel Non-Conjugated Main-Chain Hole-Transporting Polymers for Organic Electronics Application. *Macromolecular Rapid Communications* **2010,** *31* (17), 1560-1567.

19.   Choi, H.; Cho, J. W.; Kang, M.-S.; Ko, J., Stable and efficient hole transporting materials with a dimethylfluorenylamino moiety for perovskite solar cells. *Chemical Communication* **2015,** *51*, 9305-9308.

20.   Bubnova, O.; Khan, Z. U.; Wang, H.; Braun, S.; Evans, D. R.; Fabretto, M.; Hojati-Talemi, P.; Dagnelund, D.; Arlin, J.-B.; Geerts, Y. H.; Desbief, S.; Breiby, D. W.; Andreasen, J. W.; Lazzaroni, R.; Chen, W. M.; Zozoulenko, I.; Fahlman, M.; Murphy, P. J.; Berggren, M.; Crispin, X., Semi-metallic polymers. *Nature Materials* **2013,** *13*, 190.

21.   A. Lenz, H. K., A. Pohl, P. Persson, L. Ojamäe, The electronic structure and reflectivity of PEDOT:PSS from density functional theory. *Chemical Physics* **2011,** *384*, 44.

22.   Huang, C.; Fu, W.; Li, C.-Z.; Zhang, Z.; Qiu, W.; Shi, M.; Heremans, P.; Jen, A. K.-Y.; Chen, H., Dopant-Free Hole-Transporting Material with a C3h Symmetrical Truxene Core for Highly Efficient Perovskite Solar Cells. *Journal of the American Chemical Society* **2016,** *138* (2528).

23.   Gratia, P., Magomedov, A., Malinauskas, T., Daskeviciene, M., Abate, A., Ahmad, S., Grätzel, M., Getautis, V., Nazeeruddin, M. K, A Methoxydiphenylamine-Substituted Carbazole Twin Derivative: An Efficient Hole-Transporting Material for Perovskite Solar Cells. *Angewandte Chemie International Edition in English* **2015,** *54* (39), 11409.

24.   Malinauskas, T.; Saliba, M.; Matsui, T.; Daskeviciene, M.; Urnikaite, S.; Gratia, P.; Send, R.; Wonneberger, H.; Bruder, I.; Graetzel, M.; Getautis, V.; Nazeeruddin, M. K., Branched methoxydiphenylamine-substituted fluorene derivatives as hole transporting materials for high-performance perovskite solar cells. *Energy & Environmental Science* **2016,** *9*, 1681-1686.

25.   McCulloch, I.; Heeney, M.; Bailey, C.; Genevicius, K.; MacDonald, I.; Shkunov, M.; Sparrowe, D.; Tierney, S.; Wagner, R.; Zhang, W.; Chabinyc, M. L.; Kline, R. J.; McGehee, M. D.; Toney, M. F., Liquid-crystalline semiconducting polymers with high charge-carrier mobility. *Nature Materials* **2006,** *5* (4), 328.

26.   Bi, C.; Wang, Q.; Shao, Y.; Yuan, Y.; Xiao, Z.; Huang, J., Non-wetting surface-driven high-aspect-ratio crystalline grain growth for efficient hybrid perovskite solar cells. *Nat Commun* **2015,** *6*, 7747.

27.   Qin, P.; Tanaka, S.; Ito, S.; Tetreault, N.; Manabe, K.; Nishino, H.; Nazeeruddin, M. K.; Grätzel, M., Inorganic hole conductor-based lead halide perovskite solar cells with 12.4% conversion efficiency. *Nature Communications* **2014,** *5*, 3834.

28.   Shao, Y.; Xiao, Z.; Bi, C.; Yuan, Y.; Huang, J., Origin and elimination of photocurrent hysteresis by fullerene passivation in CH3NH3PbI3 planar heterojunction solar cells. *Nature Communications* **2014,** *5*, 5784.

29.   Kim, H. S.; Jang, I. H.; Ahn, N.; Choi, M.; Guerrero, A.; Bisquert, J.; Park, N. G., Control of I-V hysteresis in CH3NH3PbI3 perovskite solar cell. *Journal of Physical Chemistry Letters* **2015,** *6* (22), 4633.

Supporting information: High Mobility, Hole Transport Materials for Highly Efficient PEDOT:PSS Replacement in Inverted Perovskite Solar Cells

Materials. All reagents from commercial sources were used without further purification. Solvents were dried and purified using standard techniques. Compounds were characterized by ^{1}H NMR (400MHz), ^{13}C NMR (101MHz) on a Bruker Avance III Ultrashield 600 Plus instrument and at room temperature. High-resolution mass spectrometry (HRMS) data was recorded using a Thermo Scientific – LTQ Velos Orbitrap MS in positive atmospheric pressure photoionisation (+APPI) mode. Thermogravimetric analysis (TGA) was performed using Bruker TGA-IR TG209F1 using 10°C/min scanning rate. Differential Scanning Calorimetry (DSC) was performed on DSC-204F1 using 10°C/min scanning rate.
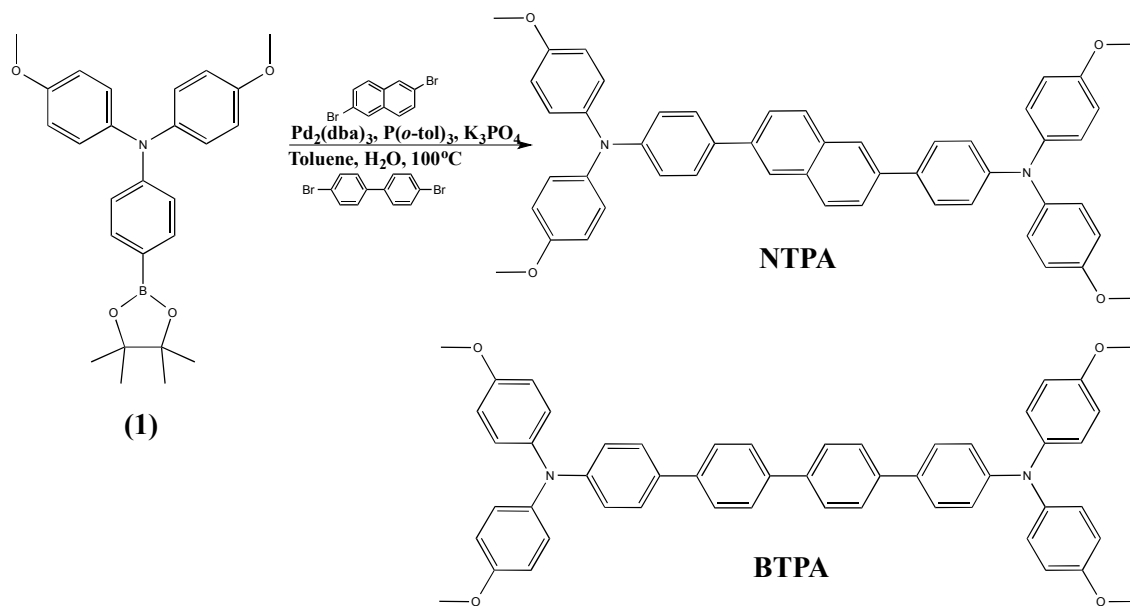
Scheme 1. Synthesis of NTPA and BTPA.

The synthesis of 4-methoxy-*N*-(4-methoxyphenyl)-*N*-(4-(4,4,5,5-tetramethyl-1,3,2-dioxaborolan-2-yl)phenyl)aniline (1) was conducted according to a modified literature procedure[1] where the crude product was recrystallized from ethanol to afford the product as a white solid. Yield (1.06g, 64%).

4,4'-(Naphthalene-2,6-diyl)bis(*N*,*N*-bis(4-methoxyphenyl)aniline)   (NTPA). Compound (1) (0.33g, 0.77mmol), 2,6-dibromonaphthalene (0.11g, 0.35mmol), Pd$_2$(dba)$_3$ (0.014g, 0.015mmol) and tri(*o*-tolyl)phosphine (0.013g, 0.042mmol)

were dissolved in degassed toluene. To this an aqueous solution of K_3PO_4 (0.37g, 1.75mmol) was added and the mixture stirred at 100°C overnight. The reaction mixture was dried with anhydrous sodium sulfate, filtered and concentrated under vacuum. The crude product was purified by column chromatography on silica gel with hexane:dichloromethane (3:1) as eluent. The product was washed with methanol, resulting in a yellow solid. Yield: 0.20g (78%)

^{1}H NMR (400MHz, d*6*-acetone) δ = 8.18 - 8.09 (m, 2H, ArH), 8.05 - 7.96 (m, 2H, ArH), 7.90 - 7.78 (m, 2H, ArH), 7.72 - 7.65 (m, 4H, ArH), 7.18 - 7.08 (m, 8H, ArH), 7.01 - 6.93 (m, 12H, ArH), 3.82 (s, 12H, OCH$_3$).

^{13}C NMR (101MHz, CD$_2$Cl$_2$) δ = 156.1, 148.3, 140.7, 137.7, 132.6, 132.4, 128.4, 127.5, 126.7, 125.4, 124.1, 120.5, 114.7, 55.4

HMRS: found: 735.3196, calcd. for C$_{50}$H$_{42}$N$_2$O$_4$ ([M+H]$^+$): 735.9079.

N[4],*N*[4],*N*[4'''],*N*[4''']-tetrakis(4-methoxyphenyl)-[1,1':4',1'':4'',1'''-quaterphenyl]-4,4'''-diamine (BTPA).

Compound (1) (0.50g, 1.16mmol), 4,4'-dibromo-1,1'-biphenyl (0.14g, 0.46mmol), Pd$_2$(dba)$_3$ (0.04g, 0.02mmol) and tri(*o*-tolyl)phosphine (0.017g, 0.06mmol) were dissolved in degassed toluene (6ml). To this an aqueous solution of K$_3$PO$_4$ (0.59g, 2.76mmol) was added and the mixture stirred at 100°C overnight. The reaction mixture was dried with anhydrous sodium sulfate, filtered and concentrated under vacuum. The crude product was purified by column chromatography on silica gel with hexane:ethyl acetate (10:1) as eluent. The product was subsequently recrystallized from ethanol, resulting in a yellow solid. Yield: 0.17g (48%)

^{1}H NMR (400MHz , d*6*-acetone) δ = 7.80 - 7.68 (m, 8 H, ArH), 7.60 - 7.53 (m, 4 H, ArH), 7.14 - 7.05 (m, 8 H, ArH), 6.93 (d, J = 8.8 Hz, 12 H, ArH), 3.80 (s, 12 H, OCH$_3$).

^{13}C NMR (101MHz, CD$_2$Cl$_2$) δ = 156.1, 148.4, 140.7, 139.5, 138.6, 132.1, 127.2, 127.1, 126.7, 126.6, 120.4, 114.7, 55.4

HMRS: found: 761.3355, calcd. for C$_{52}$H$_{44}$N$_2$O$_4$ ([M+H]$^+$): 761.9379.

1. Yu, L.; Xi, J.; Chan, H. T.; Su, T.; Antrobus, L. J.; Tong, B.; Dong, Y.; Chan, W. K.; Phillips, D. L., Novel Organic D-π-2A Sensitizer for Dye Sensitized Solar Cells and Its Electron Transfer Kinetics on TiO2 Surface. *The Journal of Physical Chemistry C* **2013,** *117* (5), 2041-2052.

Device fabrication

Patterned indium doped tin oxide (ITO) coated glass substrates (15 Ω cm^{-1}) were cleaned in an ultrasonic bath with acetone and isopropanol consecutively. Subsequently these substrates were dried with pressurised pure N$_2$ gas and treated in UV-Ozone plasma for 20 min. HTMs (10 mg/mL in 1:1 chlorobenzene (CB):ortho-dichlorobenzene (o-DCB)) were spin coated between 1000 rpm and 5000 rpm for 30 seconds and annealed at temperatures between 80˚C and 160˚C for times ranging between 0 and 20 min.

A CH$_3$NH$_3$PbI$_3$ perovskite solution was made at a concentration of 620 mg/mL; synthesis was carried out by mixing 1:1 equimolar ratios of methyl-ammonium iodide (CH$_3$NH$_3$I) purchased from DyeSol and lead (II) iodide (PbI$_2$) purchased from Alfa Aesar, in γ-butyrolactone and dimethyl sulphoxide (DMSO) in 6:4 ratio at 60˚C, the solution was left to stir until fully dissolved. The perovskite layer was spin coated at 1000 rpm for 10 seconds followed by 4000 rpm for 40 seconds with CB addition to induce fast crystallisation. The substrate was subsequently left to dry in a N$_2$ environment for 1 hour before annealing at 80˚C for 10 minutes. After annealing deposition of the PC$_{70}$BM ([6,6]-Phenyl-C71-butyric acid methyl ester) (16 mg/mL in CB) occurred, spin coating was carried out at spin speeds varying from 1200 rpm to 2250 rpm. Devices were further annealed for 2 minutes.

Subsequently 100nm of silver were thermally evaporated onto the substrates under 1x10^{-6} Torr vacuum pressure. An active area of 10mm^2 was determined by a shadow mask under evaporation conditions.

J/V device characterisation of the solar cells was preformed using a solar simulator with Xenon lamp (Oriel Instruments) calibrated to 100mW/cm^2, AM1.5G, with KG-5 silicon reference cell in a N$_2$ environment with computerised Keithley 2400 SourceMeter. External quantum efficiency (EQE) was performed by illumination of the device with Xenon arc lamp; providing monochromatic light when in combination with a dual-grating monochromator. The incident photon number was calibrated using silicon photodiode by NIST across each wavelength.

Film Characterisation

Absorption:

UV-Vis absorption spectra were obtained using a Varian Cary 5000. Photo-Electron Spectroscopy in Air (PESA) measurements were carried out at room temperature using a Riken Instruments AC-2 model to determine the ionisation potential of the HTMs. Scanning electron microscopy (SEM) images were taken at 5 V accelerating voltage and beam aperture of 30 μm, using a Zeiss Auriga microscope equipped with an in-lens detector.

Space Charge Limited Current:

In order to determine charge carrier mobility for the NTPA and BTPA, hole-only devices were fabricated with structure ITO/HTL/MoOx/Ag. Solutions of HTM were prepared in 1:1 ratios of CB:o-DCB at concentrations of 10 mg/mL and heated to 70˚C. The solutions were spin coated at varying spin speeds from 1000-5000 rpm. 8 nm of molybdenum oxide was thermally evaporated as an electron blocking layer, with a further 100 nm of silver subsequently evaporated as a cathode at 1×10^{-6} Torr vacuum pressure. An active area of 10mm^2 was determined by a shadow mask under evaporation conditions.

Hole mobilities were extracted using the modified Mott-Gurney equation below:

$$J_{SCLC} = \frac{9}{8}\varepsilon_0\varepsilon_r\mu\frac{V_{in}^2}{L^3}e^{\left(\frac{0.89\beta}{\sqrt{L}}\sqrt{V_{in}}\right)}$$

where J$_{SCLC}$ is the measured current density, ε$_0$ and ε$_r$ are defined as the vacuum permittivity and material dielectric constant respectively, L is the film thickness, μ the hole mobility, and β is the field activation parameter.

Hysteresis
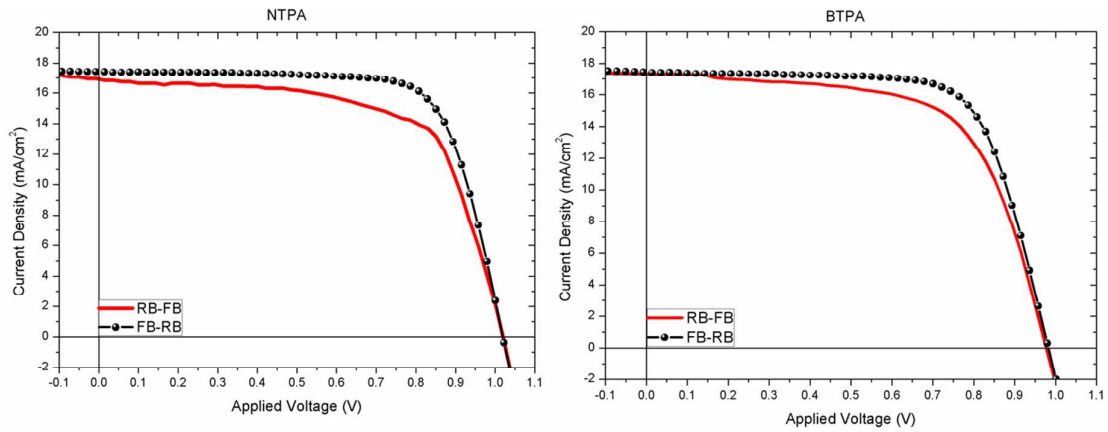
Figure S1: J/V characteristics of perovskite devices with NTPA and BTPA measured in both Reverse-Forward Bias (RB-FB) and Forward-Reverse (FB-RB).

Device statistics
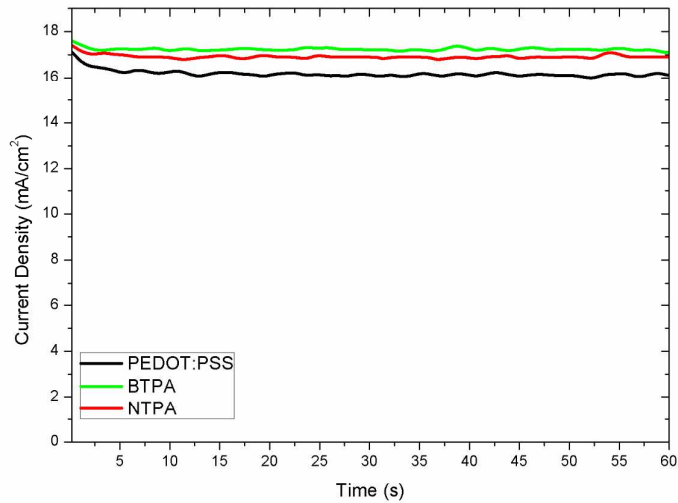
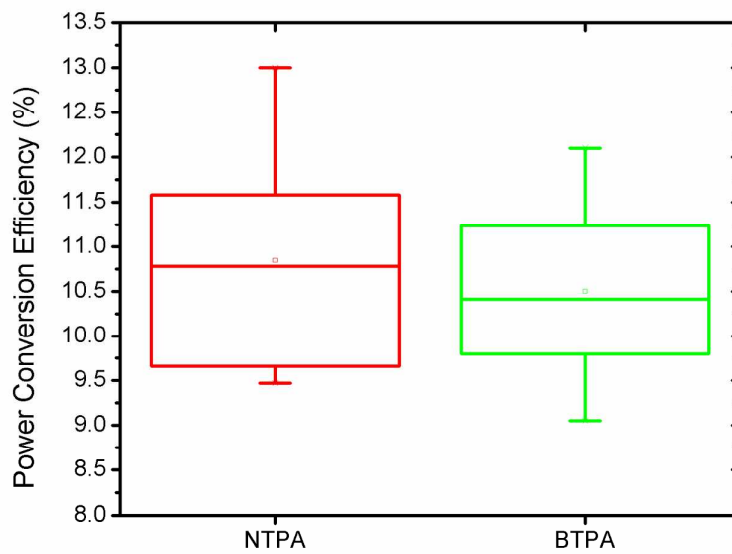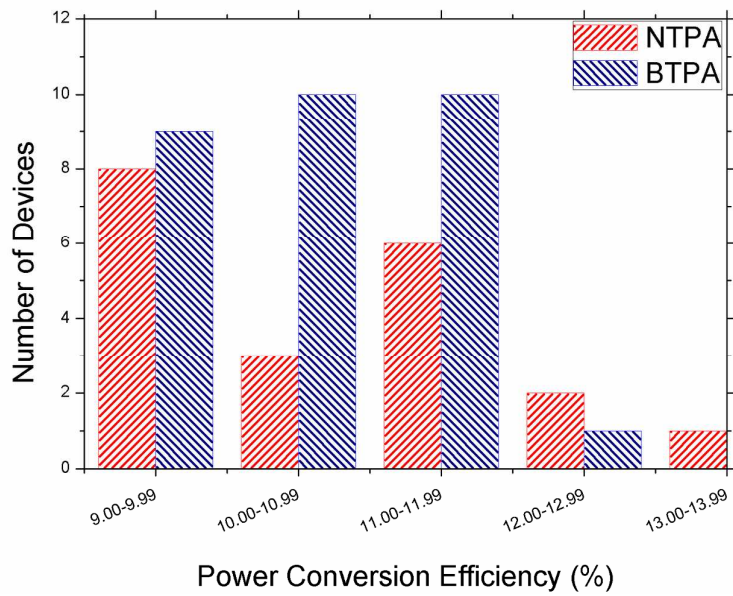Figure S2: Current stability over time at Maximum Power Point (M_{PP}).

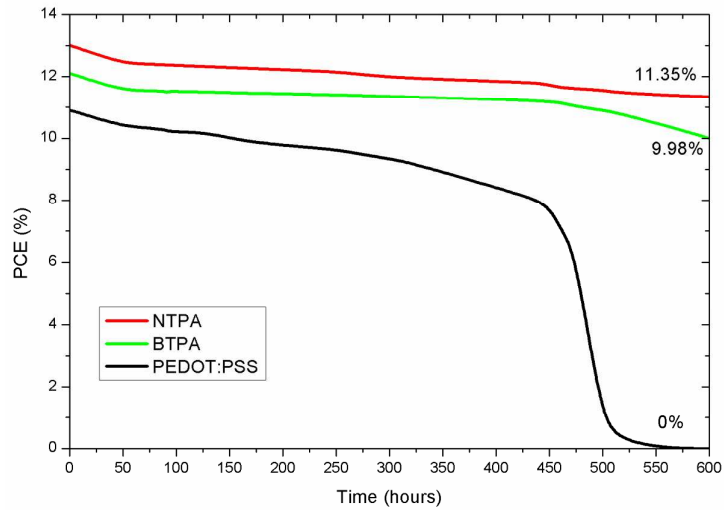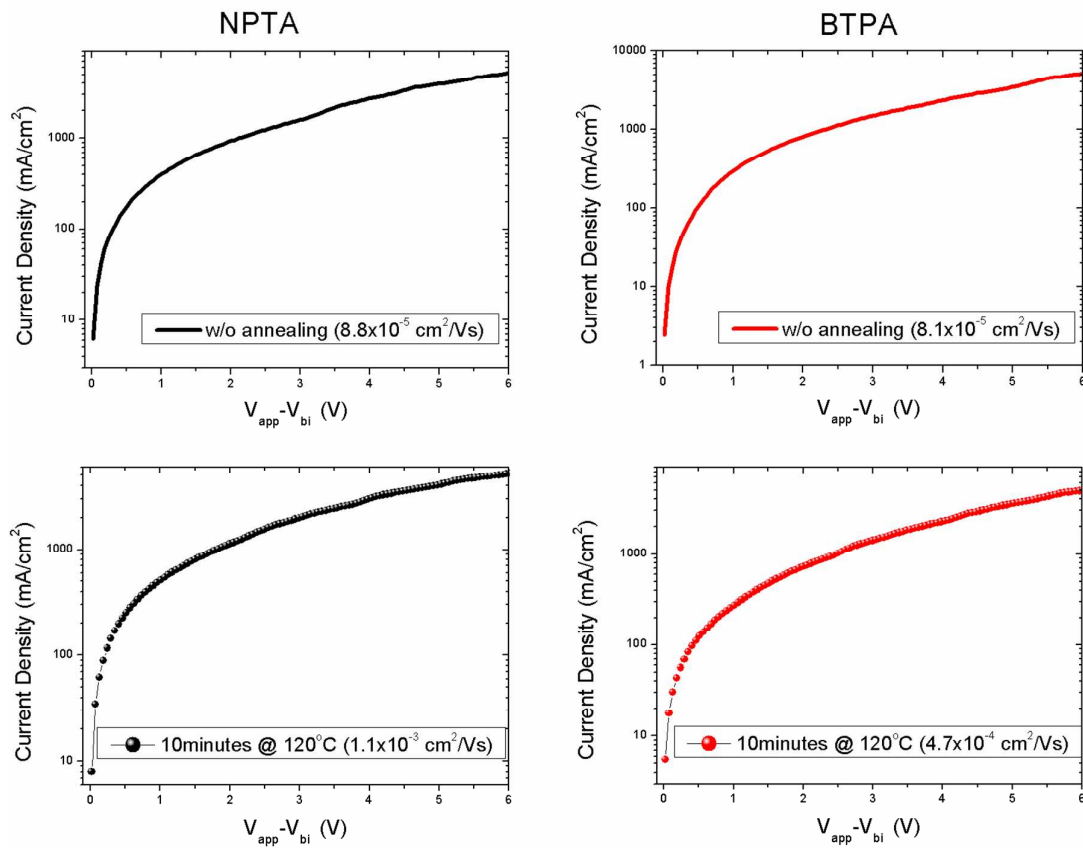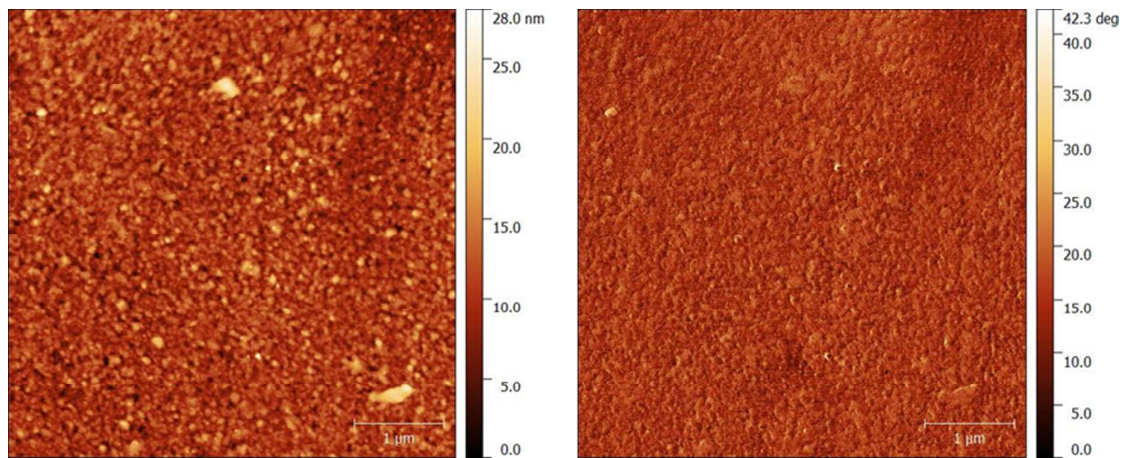Figure S3(a), (b): Device statistics.

Figure S4: Lifetime measurements and PCE evolution.

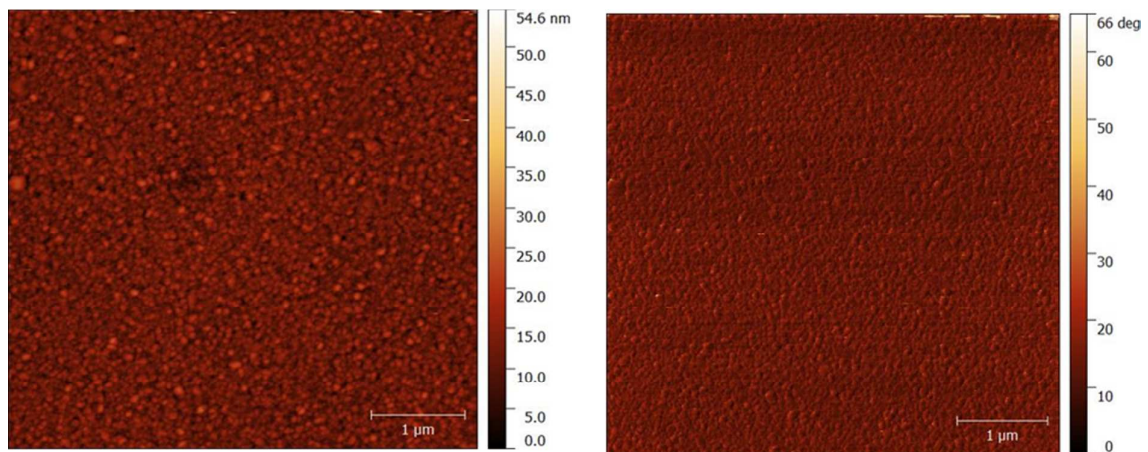Figure S5: SCLC mobility measurements for NTPA and BTPA.

BTPA.

NTPA.

Figure S6: AFM of NTPA and BTPA layers showing height and phase of annealed devices.
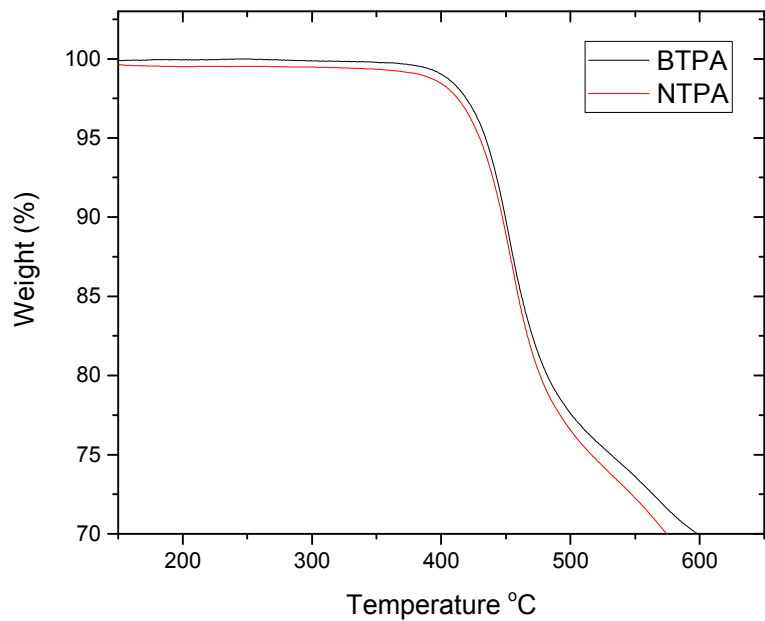
Figure S7: TGA curves of NTPA and BTPA.
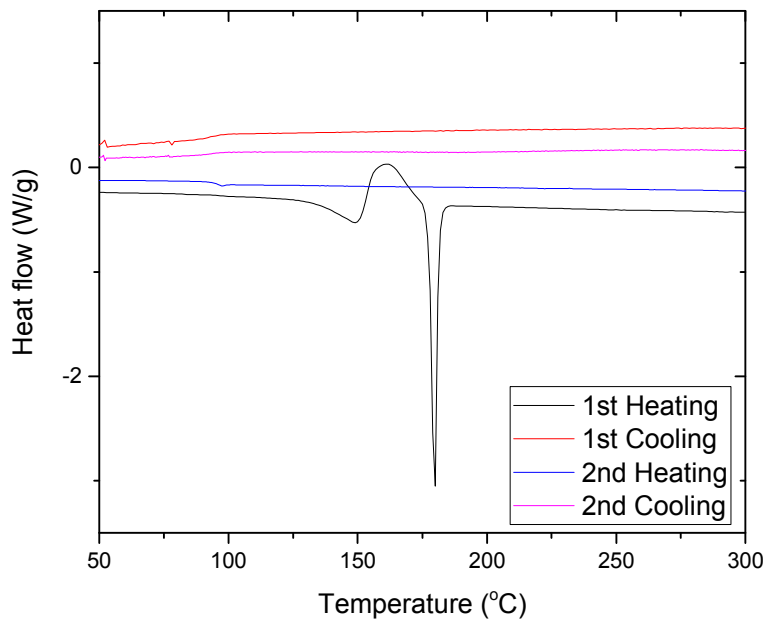
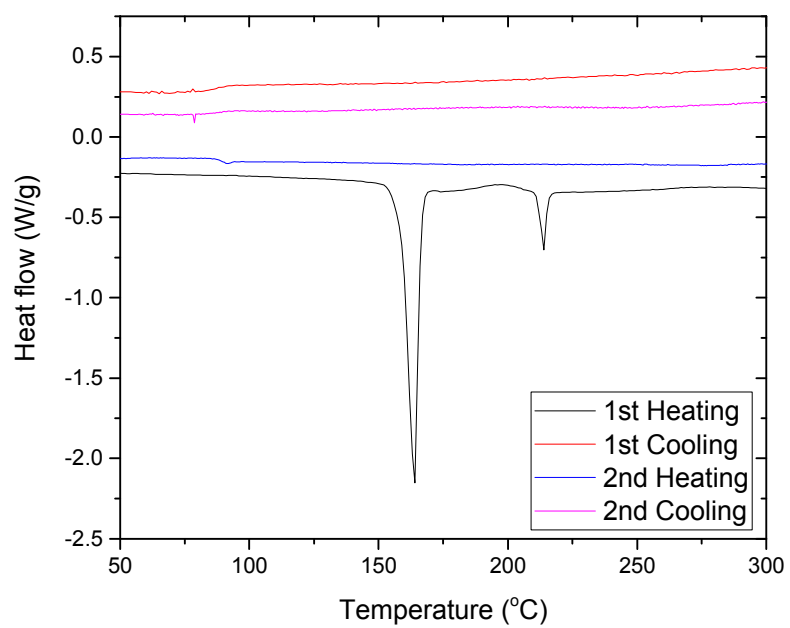

Figure S8: DSC curves of NTPA.
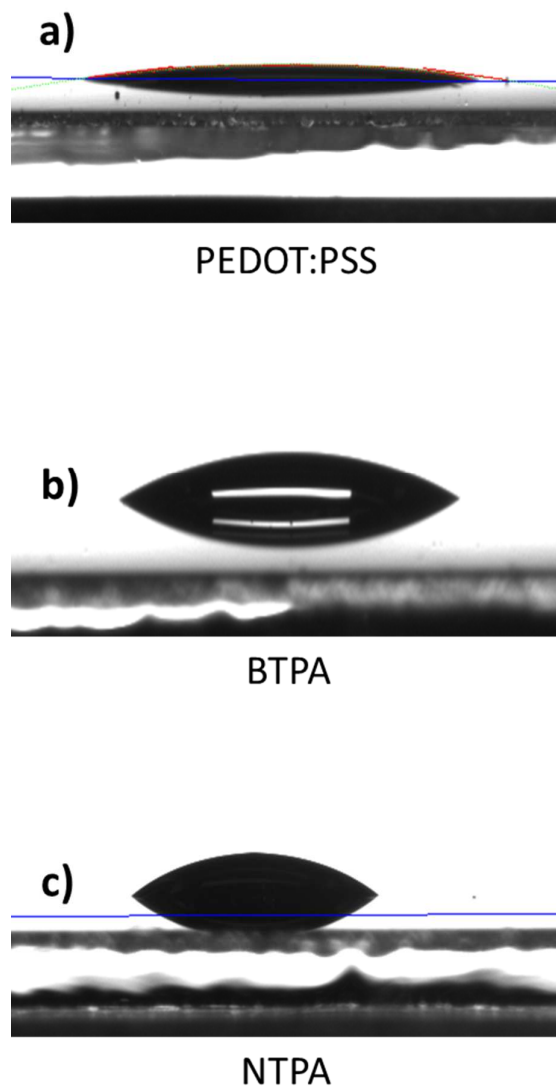
Figure S9: DSC curves of BTPA.

Figure S10. Contact angle of perovskite droplets on top of a) PEDOT:PSS, b) BTPA and c) NTPA with measured angles 5.6°, 17.9° and 45.5° respectively.
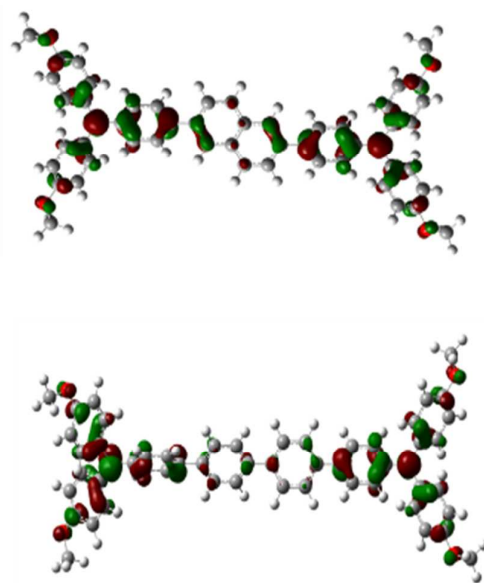
DFT calculations

Figure S11. DFT calculations for the in-use molecules

Density functional theory (DFT) calculations were carried out with Gaussian at the B3LYP/6-31g* level of theory in gas phase to determine the energy-minimized molecular conformations and to visualize the HOMO and LUMO spatial distributions. Images were generated with the GaussView software package.